Supporting Information

Modulating Optoelectronic Properties of Two-Dimensional Transition Metal Dichalcogenide Semiconductors by Photoinduced Charger Transfer

Jungwook Choi, Hanyu Zhang, and Jong Hyun Choi*

School of Mechanical Engineering, Purdue University
West Lafayette, Indiana 47907, United States

*Email: jchoi@purdue.edu

Contents:

1. PL spectra of TMDCs before and after annealing

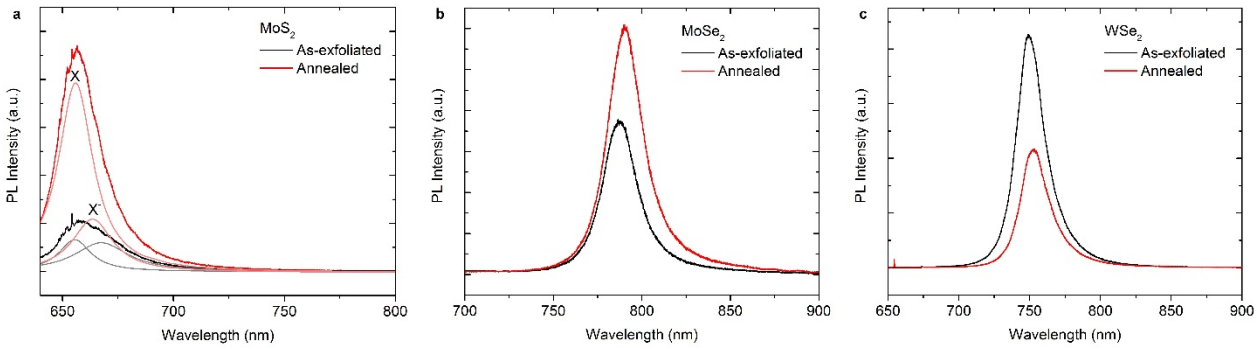

Figure S1. PL spectra of monolayer (a) MoS_2, (b) $MoSe_2$, and (c) WSe_2 excited before and after annealing and subsequent air exposure. A 633-nm HeNe laser was used for excitation and measurements were performed at room temperature. The PL of TMDCs is dominated by exciton recombination. The MoS_2 PL may be deconvoluted into two emission maxima of excitons (X) and negatively charged excitons (negative trions, X^-) at room temperature as fitted by two Lorentzian functions in (a). For $MoSe_2$ and WSe_2, the charged exciton emission is observed only at low temperature. Thus, the formation of excitons and trions in emission spectra can be studied using MoS_2 at the room temperature. The thermal annealing process may remove adsorbates and contaminants on the MoS_2 layer. Once the MoS_2 is exposed to ambient air after annealing, atmospheric molecules such as oxygen can interact with the fresh surface, depleting abundant electrons in MoS_2 due to its strong electronegativity.[1,2] This electron transfer results in suppression of formation of negative trions and thus increase exciton emission. Therefore, the intensity of overall PL spectra is enhanced with increased excitonic recombination (red curve in (a)). Similar PL enhancement is also observed in the $MoSe_2$, which is another n-type electron-rich semiconductor, after annealing and air exposure. In contrast, p-type WSe_2 that lacks excessive electrons shows opposite behaviors as in (c).[1] The decrease/increase in PL emission spectra before and after annealing implies the significant role of electrons that natively exist in the TMDCs, and thus most chemical doping methods rely on modulation of those excessive electrons for PL tuning.[3–5] In this work, the excessive electrons in TMDCs are already transferred after annealing and air exposure, thereby enabling PL modulation *via* photoinduced charge transfer. Note that the annealing temperature was 250 °C which was lower than the temperature that would generate the defects in the TMDCs (*e.g.*, 500 °C).[6] Therefore, the defects may not play a critical role in PL modulation in our study.

2. Effects of solvent on the optical characteristics of TMDCs

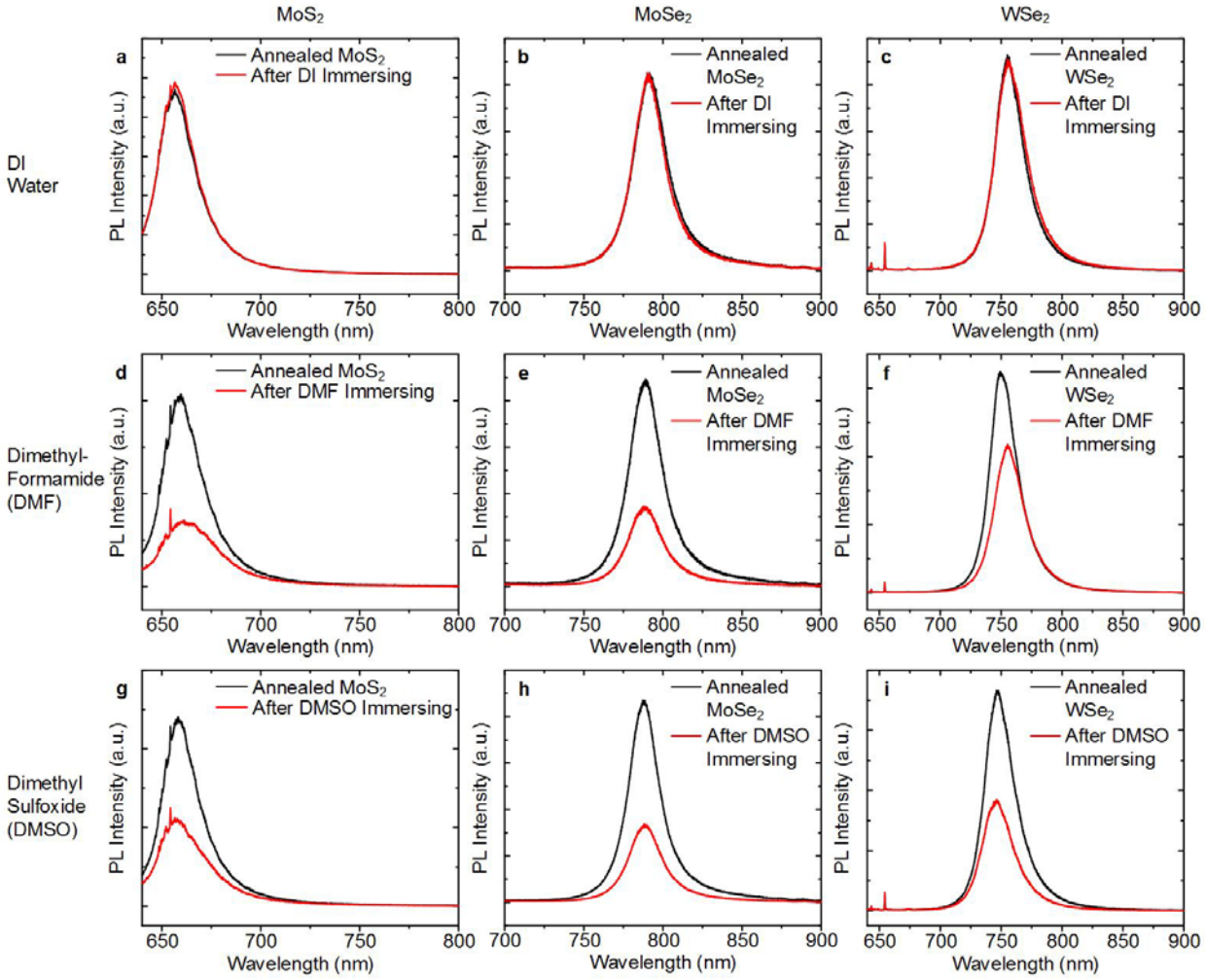

Figure S2. The PL spectra of MoS_2, $MoSe_2$, and WSe_2 monolayers before and after immersion in (a–c) DI water, (d–f) dimethylformamide (DMF), and (g–i) dimethyl sulfoxide (DMSO). After mechanical exfoliation of TMDCs on the SiO_2/Si substrate, all TMDC layers were annealed in argon at atmospheric pressure at 250 °C for 1 h. Then, the TMDCs were immersed in DI water, DMF, or DMSO for 10 min, followed by rinsing with DI water and blow-drying with air. While DI water has little effects on the PL of TMDCs (a–c), DMF and DMSO quench the PL of TMDCs significantly (d–i), likely due to the methyl group ($-CH_3$) in the solvents that attracts electrons. As a result, the carrier density in the TMDC layers changes and excitonic recombination is suppressed. In order to exclude any possible solvent effects, we used only DI water for dissolving MPcs throughout the work.

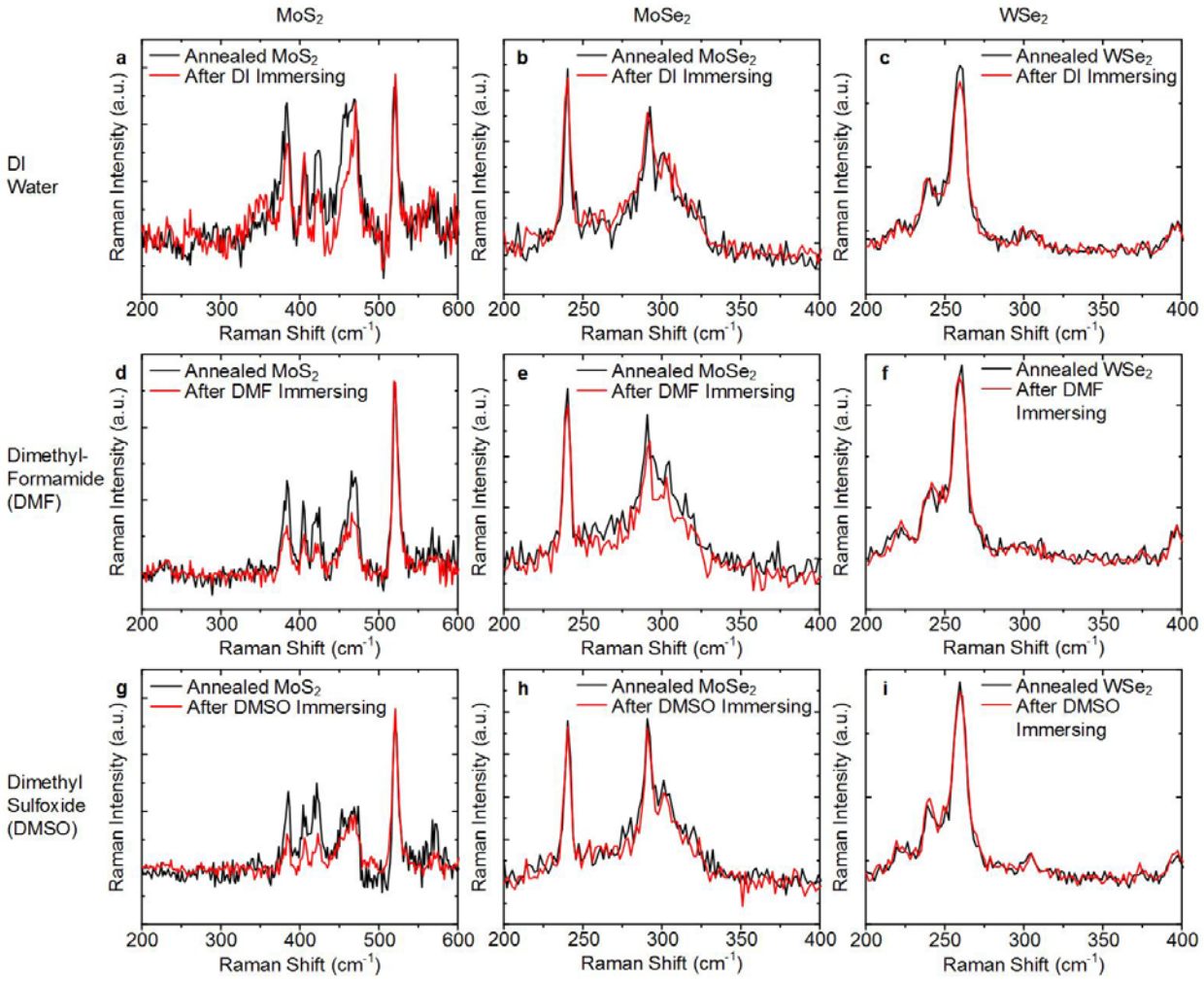

Figure S3. The Raman spectra of MoS_2, $MoSe_2$, and WSe_2 before and after immersion in (a–c) DI water, (d–f) DMF, and (g–i) DMSO. In contrast to the PL, there is no significant change in the Raman signatures after immersion in the solvents.

3. Raman spectra of NiPc and MgPc

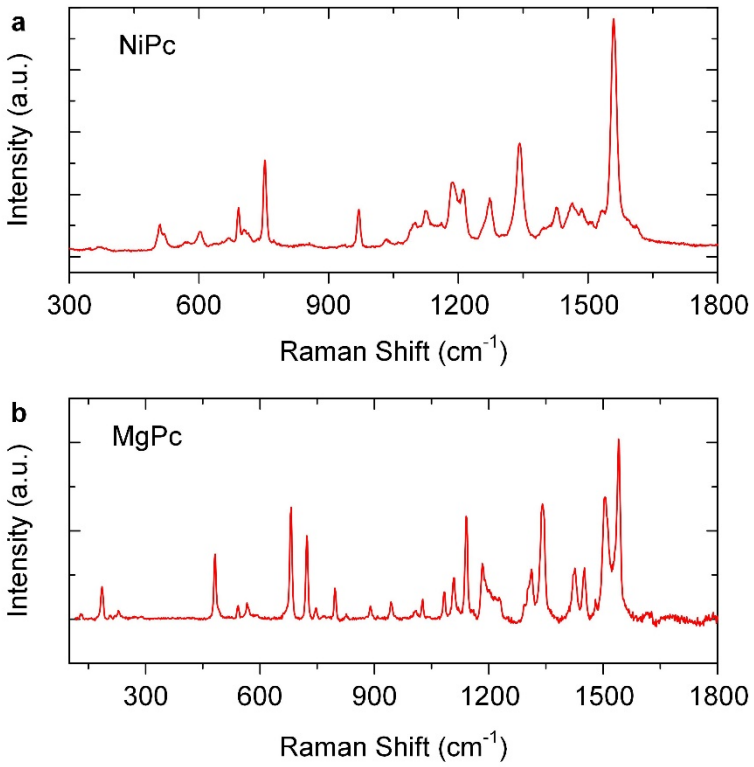

Figure S4. Raman spectra of (a) NiPc and (b) MgPc (with 633 nm excitation) show several signatures. A 10-μL aliquot of 1 mM NiPc or the MgPc solution was drop-casted on the surface of SiO_2, and the Raman spectra were collected after DI water evaporation (after 1 hour). The pathalocyanine signatures are consistent with previous reports.[7,8]

4. XPS spectra of TMDCs with and without NiPc

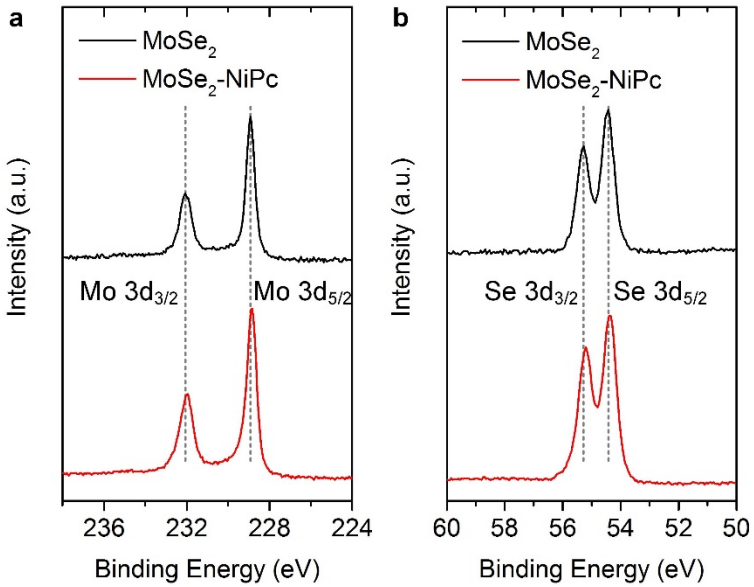

Figure S5. Mo 3d and S 2p core level XPS spectra of $MoSe_2$ with and without NiPc, showing little changes after functionalization.

		Binding energy (eV)	
		Pristine TMDCs	**NiPc-functionalized TMDC**
MoS_2	Mo $3d_{5/2}$	229.27	229.20
	Mo $3d_{3/2}$	232.40	232.32
	S 2s	226.39	226.33
	S $2p_{3/2}$	162.08	162.02
	S $2p_{1/2}$	163.24	163.18
$MoSe_2$	Mo $3d_{5/2}$	228.92	228.85
	Mo $3d_{3/2}$	232.02	231.97
	Se $3d_{5/2}$	54.43	54.37
	Se $3d_{3/2}$	55.27	55.20
WSe_2	W $4f_{7/2}$	32.29	32.23
	W $4f_{5/2}$	34.43	34.37
	Se $3d_{5/2}$	54.55	54.48
	Se $3d_{3/2}$	55.36	55.30

Table S1. Summary of XPS binding energies of MoS_2, $MoSe_2$, and WSe_2 with and without NiPc. A shift of binding energy in XPS spectra would indicate the offset of Fermi level, which may be used as a measure of determining the extent of doping in the TMDCs.[9] Previous studies reported that chemical doping by surface charge transfer results in the binding energy shift in the range of 0.3–0.8 eV.[5,9,10] Our XPS spectra reveal minimal doping effects with binding energy shifts less than 0.07 eV. We observe a slight deviation in binding energies of Mo 3d and Se 3d between MoS_2 and $MoSe_2$ (~0.35 eV) and between $MoSe_2$ and WSe_2 (~0.1 eV). This discrepancy could be due to local variations in stoichiometry and defects, resulting in different XPS spectra even in the same flake.[11,12]

5. AFM, PL, and Raman studies on the TMDCs functionalized with naphthalene and F_4TCNQ

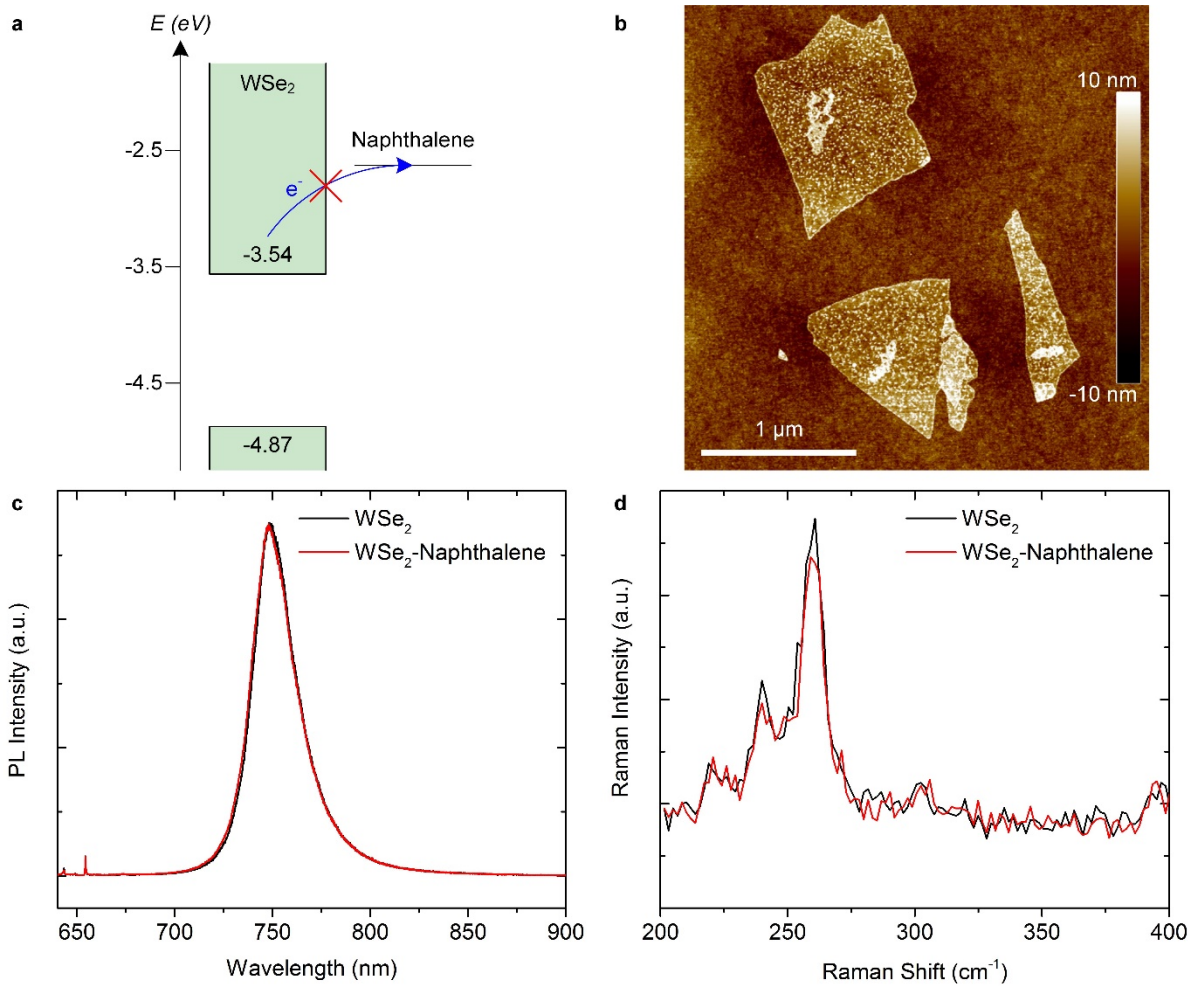

Figure S6. AFM, PL, and Raman characterization of naphthalene derivative-functionalized monolayer WSe_2. Approximately 100 μM sodium 2-naphthalenesulfonate (NS) was dissolved in DI water, and annealed WSe_2 flakes were subsequently submerged in the solution for 20 min. Then, the sample was rinsed by DI water and dried by air. (a) Relative energy offset between the band edges of monolayer WSe_2 and the typical reduction potential of naphthalene derivatives. The reduction potential of NS is unknown to the best of our knowledge, but it should be positioned well above CBM of WSe_2. For example, the reduction potential of naphthalene-1,5-disulfonate and naphthalene-1,2-dimethyl is around -2.59 and -2.23 eV, respectively.[13] Therefore, the photoinduced charge transfer from the WSe_2 to naphthalene is not energetically favorable. (b) AFM height image of NS-functionalized WSe_2 flakes. (c) PL spectra of pristine WSe_2 and NS-functionalized WSe_2. Because excited electrons in the WSe_2 are not allowed to transfer to NS, excitonic recombination is not altered, resulting in no change of PL. (d) Raman spectra of WSe_2 before and after NS functionalization, showing nearly identical signatures. It is noted that the pristine WSe_2 flake was immersed in DI water without NS for 20 min and dried before PL and Raman measurement as a control. The results support the photoinduced charge transfer mechanism in MPc-functionalized TMDCs.

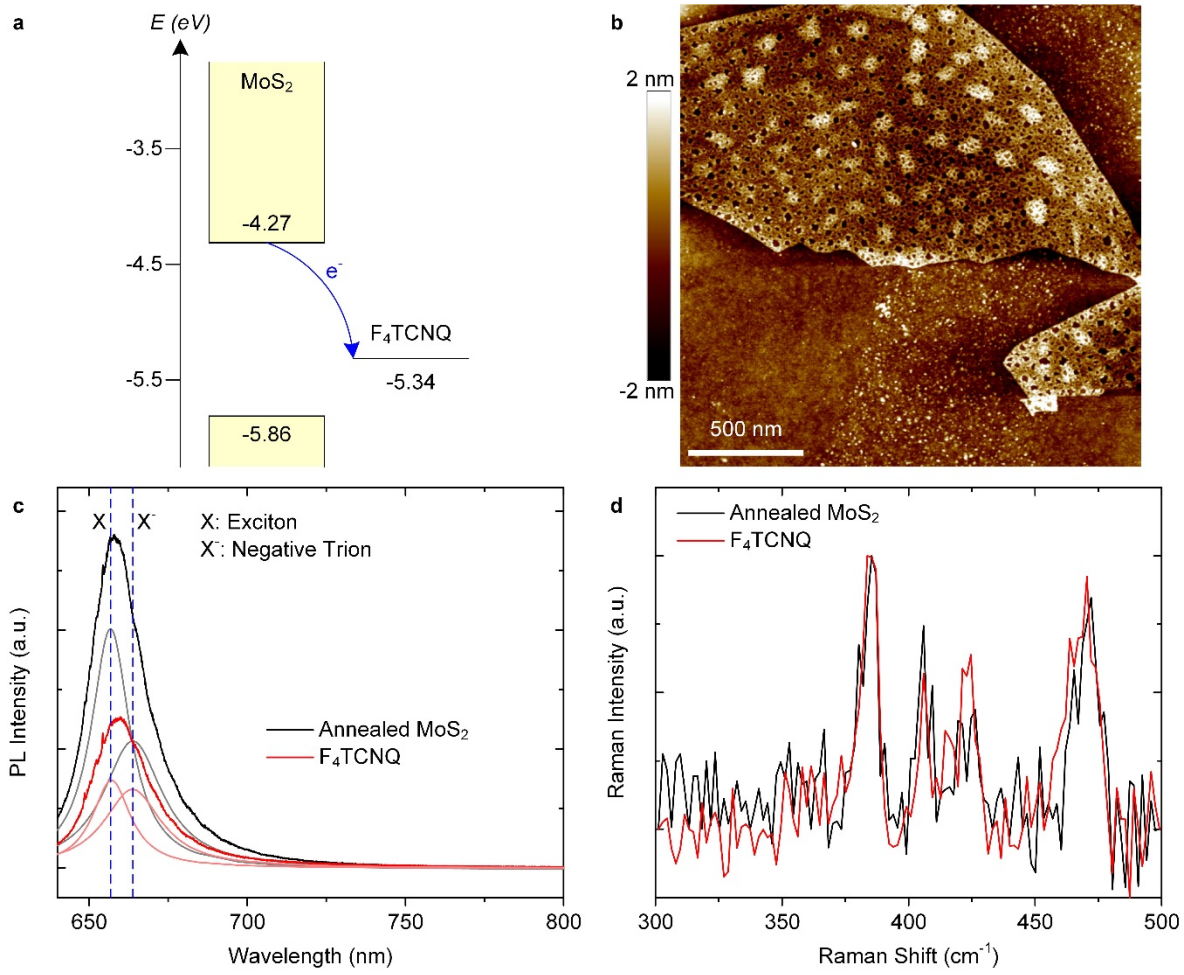

Figure S7. AFM, PL, and Raman characterization of monolayer MoS_2 functionalized with 2,3,5,6-tetrafluoro-7,7,8,8-tetracyanoquinodimethane (F_4TCNQ). Approximately 1 mM F_4TCNQ was dissolved in DI water, and an annealed MoS_2 layer was incubated in the solution for 20 min, followed by DI water rinsing and air-drying. (a) The reduction potential of F_4TCNQ is located between the band edges of MoS_2,[3,4] such that photoexcited electrons can be transferred from MoS_2 to F_4TCNQ. (b) AFM height image of F_4TCNQ-functionalized MoS_2. (c) PL spectra of pristine MoS_2 and F_4TCNQ-functionalized MoS_2. Due to the photoinduced charge transfer, exciton recombination is diminished, resulting in PL quenching. The intensity of exciton peak is significantly decreased after functionalization, and spectral weight of exciton (intensity of exciton emission divided by total intensity of PL) decreases from 0.72 to 0.58. This result is contrast to a previous report,[3] where the exciton emission increased after F_4TCNQ functionalization by the transfer of excessive electrons and the resulting decrease of negative trion formation. In our experimental conditions, the abundant electrons MoS_2 are depleted through annealing and air exposure before functionalization, and thus, photoinduced charge transfer mechanism can dominate the PL response. (d) Raman spectra of MoS_2 before and after F_4TCNQ functionalization, showing nearly identical signatures. It is noted that the pristine MoS_2 was immersed in DI water without F_4TCNQ for 20 min and dried before PL and Raman measurements as a control.

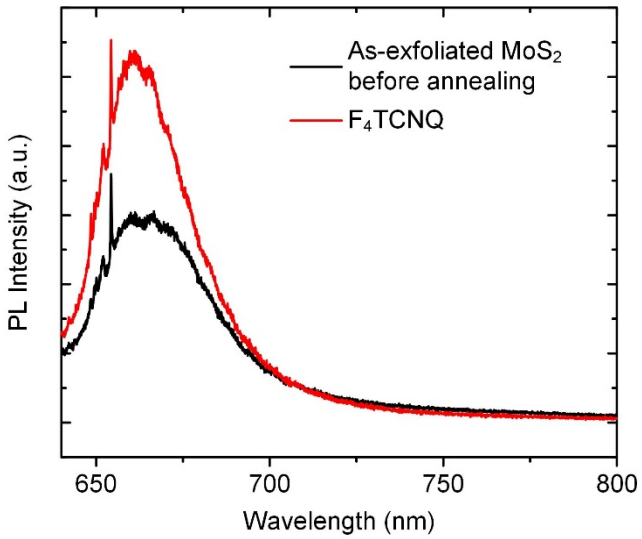

Figure S8. PL spectra of as-exfoliated MoS_2 and F_4TCNQ-functionalized MoS_2. In contrast to the annealed MoS_2-F_4TCNQ in Figure S7 that shows the PL quenching, the PL intensity of as-exfoliated MoS_2 increases after functionalization of F_4TCNQ. It is attributed to the depletion of excessive electrons and thereby decreased formation of negative trions, which is consistent with previous report.[3] The opposite emission behaviors with the same functional molecules indicate the importance of initial state of TMDCs. In our experiments, the PL modulation is determined by the amount of excessive electrons in the native TMDCs.

6. Raman spectra of TMDCs and MPc-functionalized TMDCs

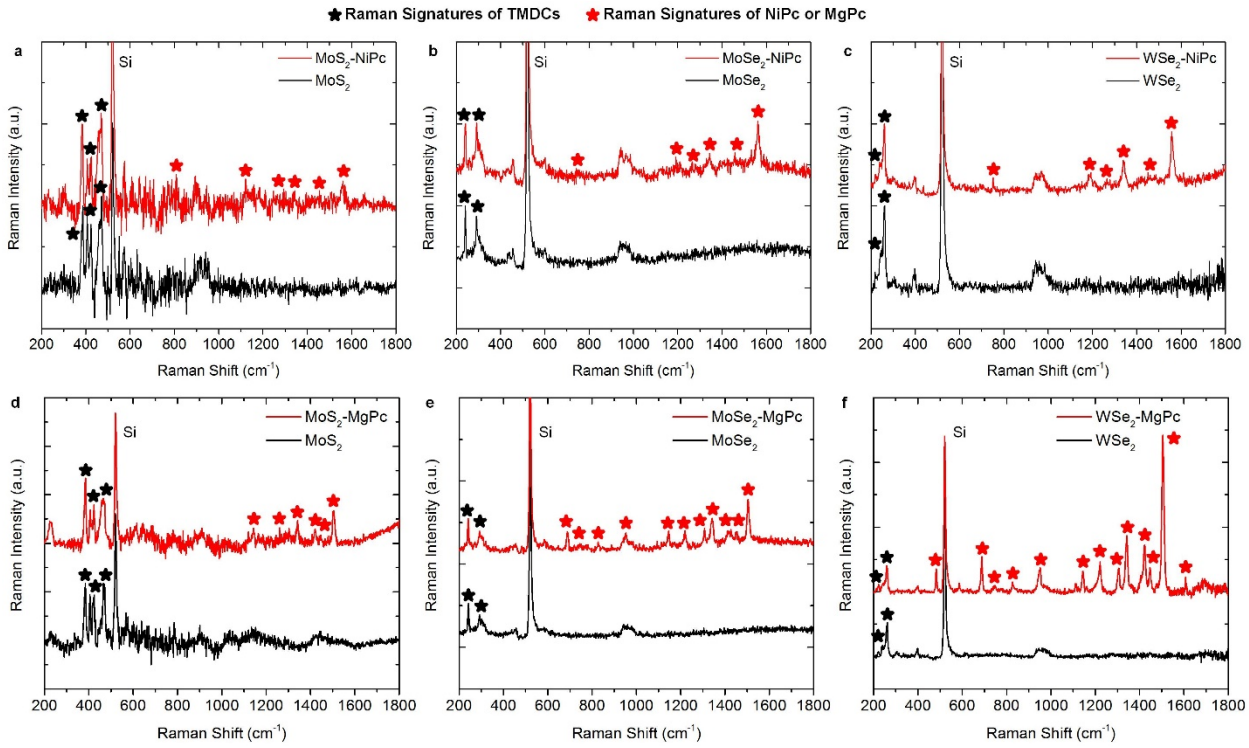

Figure S9. Raman spectra of (a) MoS_2 and MoS_2-NiPc, (b) $MoSe_2$ and $MoSe_2$-NiPc, (c) WSe_2 and WSe_2-NiPc, (d) MoS_2 and MoS_2-MgPc, (e) $MoSe_2$ and $MoSe_2$-MgPc, and (f) WSe_2 and WSe_2-MgPc. Black stars indicate the Raman modes of the TMDCs, and red stars represent the Raman signatures of the MPcs. Both spectra of pristine TMDCs and MPc-functionalized TMDCs are collected from the same flakes before and after functionalization, indicating successful functionalization.

7. PL quenching of multilayer WSe_2 after NiPc functionalization

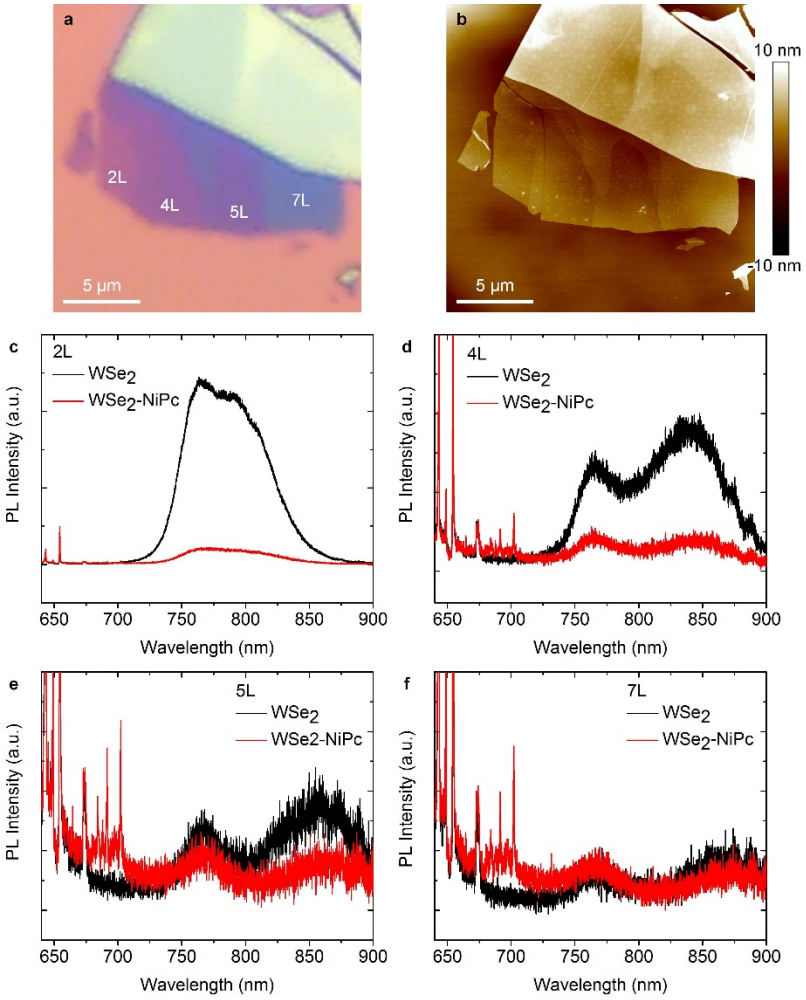

Figure S10. PL spectra of WSe_2 with various thickness ranging from 2 to 7 layers before and after NiPc functionalization. (a) Optical microscope image of the WSe_2 flake. (b) AFM height image of the same WSe_2 flake shown in (a). (c–f) PL spectra of 2L (c), 4L (d), 5L (e), and 7L (f) WSe_2 before and after functionalization. In contrast to monolayer WSe_2 where CBM and VBM coincide at the K point, the multilayer WSe_2 has upshifted valence band at the Γ point and downshifted conduction band at the Λ point.[14] The local shift of conduction and valence bands makes them indirect bandgap semiconductors. The emission from direct (indirect) bandgap transitions are located at 759.7 (791.8), 767.6 (836.1), 767.7 (857.6), and 767.7 nm (872.6 nm) for 2L, 4L, 5L and 7L, respectively. After NiPc functionalization, the PL quenches regardless of origin of emission due to photoinduced excited electron transfer from the WSe_2 to the NiPc. It is noted that several Raman signatures from NiPc are also shown in (c–f) after functionalization, which are located at 702.2 (1561.8), 691.6 (1343.6), 688.1 (1270), 684 (1182.9), and 664.5 nm (753.9 cm^{-1}).

8. AFM image, PL and Raman maps of MPc-functionalized TMDCs

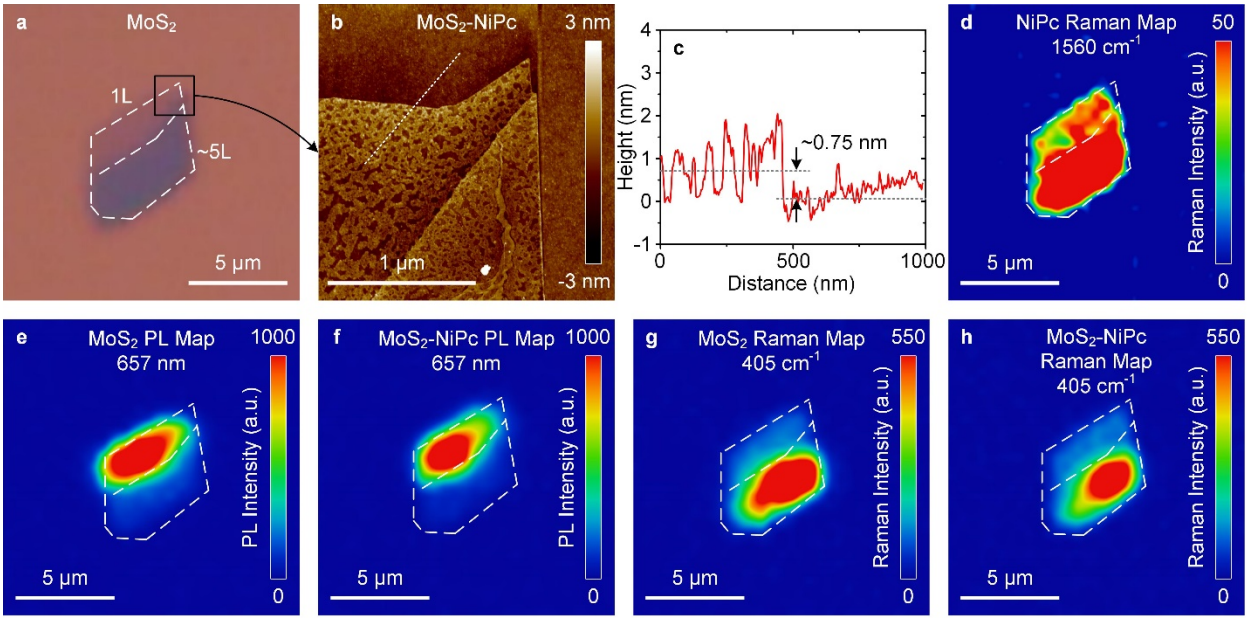

Figure S11. Characterizations of MoS_2 before and after NiPc functionalization. (a) Optical microscope image of 1L and 5L MoS_2. (b) AFM image measured after NiPc functionalization. (c) AFM height profile obtained along the white dotted line in (b). (d) Raster-scanned Raman intensity map of NiPc at 1560 cm^{-1} corresponds the shape of the MoS_2 flake, indicating selective and uniform functionalization of NiPc on MoS_2. (e,f) PL intensity map of MoS_2 at 657 nm before (e) and after (f) NiPc functionalization. No significant PL quenching after functionalization supports the photoinduced charge transfer mechanism where the photoexcited electrons in MoS_2 are not allowed to transfer to the NiPc. (g,h) Raman intensity map of MoS_2 at 405 cm^{-1} before (g) and after (h) NiPc functionalization, showing no change in the Raman signature.

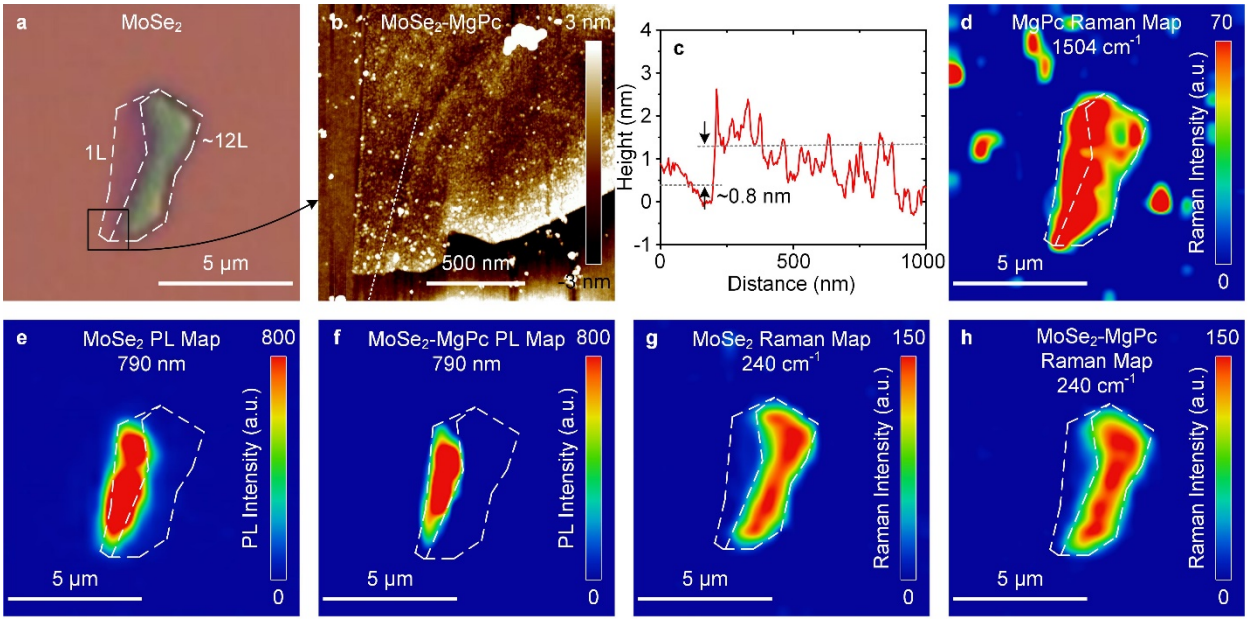

Figure S12. Characterization of $MoSe_2$ before and after MgPc functionalization. (a) Optical microscope image of 1L and 12L $MoSe_2$. (b) AFM image measured after MgPc functionalization. (c) AFM height profile obtained along the white dotted line in (b). (d) Raster-scanned Raman intensity map of MgPc at 1504 cm^{-1} corresponds the shape of the $MoSe_2$ flake. Due to relatively low water solubility of MgPc, several MgPc aggregates are found on the surface of SiO_2. (e,f) PL intensity map of $MoSe_2$ at 790 nm before (e) and after (f) MgPc functionalization. No significant PL quenching after functionalization supports the photoinduced charge transfer mechanism where the photoexcited electrons in $MoSe_2$ are not allowed to transfer to the MgPc. (g,h) Raman intensity map of $MoSe_2$ at 240 cm^{-1} before (g) and after (h) MgPc functionalization, showing no change in the Raman signature.

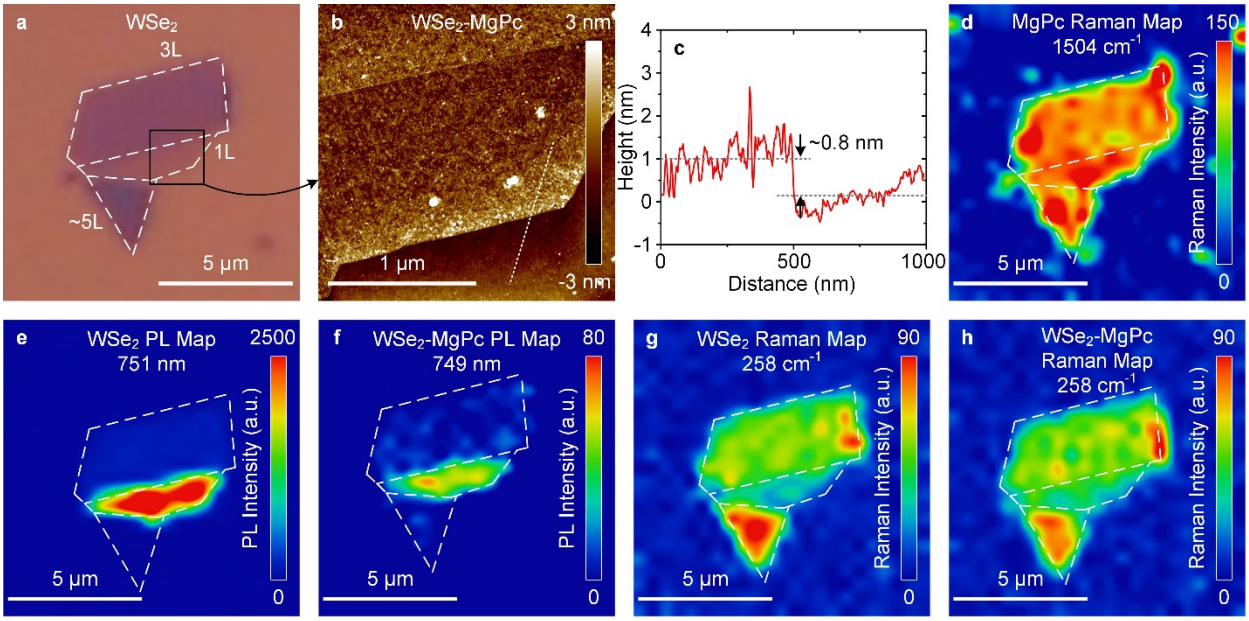

Figure S13. Characterization of WSe_2 before and after MgPc functionalization. (a) Optical microscope image of 1L, 3L and 5L WSe_2. (b) AFM image measured after MgPc functionalization. (c) AFM height profile obtained along the white dotted line in (b). (d) Raster-scanned Raman intensity map of MgPc at 1504 cm^{-1} corresponds the shape of the WSe_2 flake. (e,f) PL intensity map of WSe_2 before (at 751 nm) (e) and after (at 749 nm) (f) MgPc functionalization. The WSe_2 PL is quenched and blue-shifted after MgPc functionalization. Because the photoexcited electrons in WSe_2 are allowed to transfer to the MgPc, the recombination diminishes, resulting in significant PL quenching. (g,h) Raman intensity map of WSe_2 at 258 cm^{-1} before (g) and after (h) MgPc functionalization, showing no change in Raman signature.

9. Static PL quenching of WSe_2 with NiPc

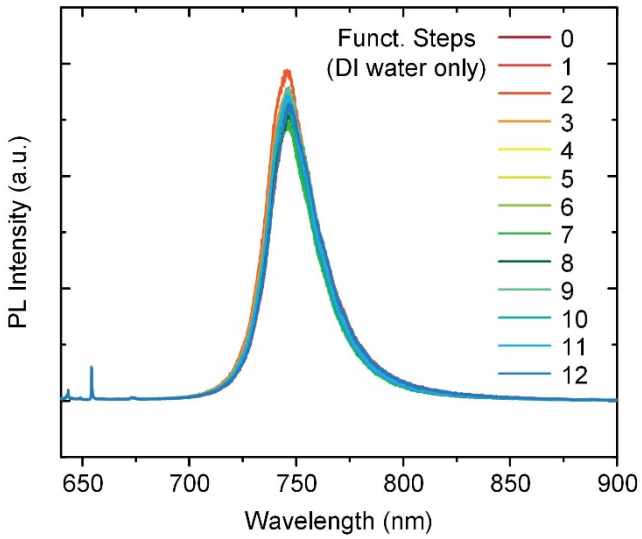

Figure S14. Monolayer WSe_2 was annealed and immersed in DI water for 5 min without NiPc molecules for each step, which is identical to the functionalization steps presented in Figure 4a. The PL does not quench throughout the experiments, indicating negligible effects of DI water.

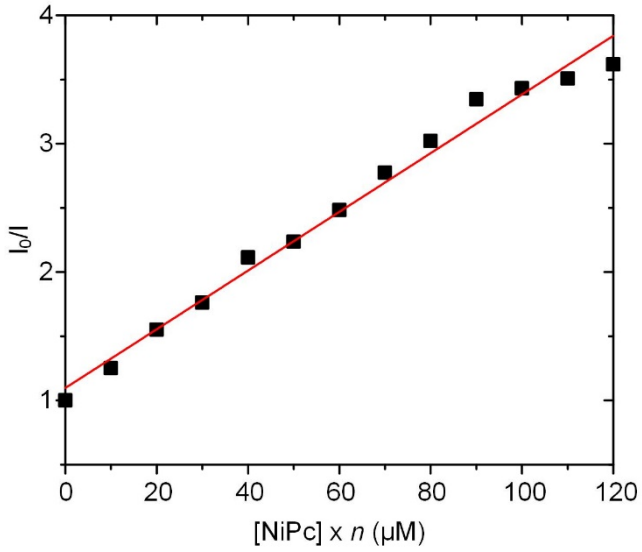

Figure S15. WSe_2 PL quenching with increasing functionalization step. We assumed that the NiPc concentration increases linearly with the number of functionalization steps. For each functionalization step, the WSe_2 was immersed in NiPc solution ([NiPc] = 10 μM) for 5 min, followed by DI rinsing and drying. The quenching behavior follows a static quenching equation, $I_0/I = 1 + Kn$[MPc], where I and I_0 are the PL intensity with and without quencher (NiPc in this case), K is the association constant, and n is the number of functionalization step. The association constant ($K = 2.3 \times 10^4$ M^{-1}) can be estimated from the linear relation between the I_0/I and the increasing functionalization step of NiPc.

10. Analysis of *I–V* curves measured using PC-AFM

We measured the current transport behaviors of WSe_2 and WSe_2-NiPc in dark and under illumination using PC-AFM. The experimental data was fitted to the thermionic emission model[15] as presented in Figure 5b and c in the main text. The current I and saturation current I_0 are given by:

$$I = I_0\left[\exp\left(\frac{qV}{\eta k_B T}\right) - 1\right]$$

$$I_0 = A_e A^* T^2 \exp\left(-\frac{q\Phi_B}{k_B T}\right)$$

where q is the electronic charge, V is the applied bias voltage, η is the ideality factor, k_B is the Boltzmann constant, Φ_B is the barrier height, A_e is the effective contact area, A^* is the Richardson constant, and T is the temperature. From the contact force (~20 nN) that we used during the PC-AFM measurements, the effective contact area (A_e) was estimated to be roughly 5 nm^2.[16] The Richardson constant (A^*) can be expressed as:

$$A^* = \frac{4\pi q m^* k_B^2}{h^3}$$

where m^* is the effective electron mass and h is the Planck constant. For free electrons ($m^* = m_0$, where m_0 is the electron mass), the Richardson constant is 120 A cm^{-2} K^{-2}.[15] The ideality factor (η) can be estimated from the slope of the linear relation in $dV/d(\ln I)$:

$$\frac{1}{\eta} = \frac{k_B T}{q}\frac{d(\ln I)}{dV}$$

and the saturation current (I_0) can be obtained by fitting the experimental data to the thermionic emission model. Finally, we can calculate the barrier height from the equation below:

$$\Phi_B = \frac{k_B T}{q}\ln\left(\frac{A_e A^* T^2}{I_0}\right)$$

Estimated barrier height from the thermionic emission model is 0.17 and 0.21 eV for forward and reverse bias in dark, and 0.15 and 0.18 eV for forward and reverse bias under illumination. After NiPc functionalization, the barrier height is estimated to be 0.18 and 0.21eV for forward and reverse bias in dark, and 0.13 and 0.12 eV for forward and reverse bias under illumination. The obtained barrier height is slightly smaller than the value obtained from the band alignment (~0.2 eV) in Figure S16a, possibly due to tunneling current which is not considered in the thermionic model.[16] Nevertheless, the decreased barrier height under illumination corresponds to the increased current flow by the contribution of photo-generated carriers, and it is more significant when the WSe_2 is functionalized with NiPc which facilitates charge separation.

The fitting results are plotted in semi-log *I–V* curves as shown in Figure 16b, which shows typical p-type transport behavior.[11] In dark condition, the *I–V* curves are similar before and after NiPc functionalization, indicating the NiPc does not disturb current flow. However, under

illumination, the NiPc-functionalized WSe_2 shows improved photocurrent than the pristine WSe_2, as clearly seen in Figure 16b.

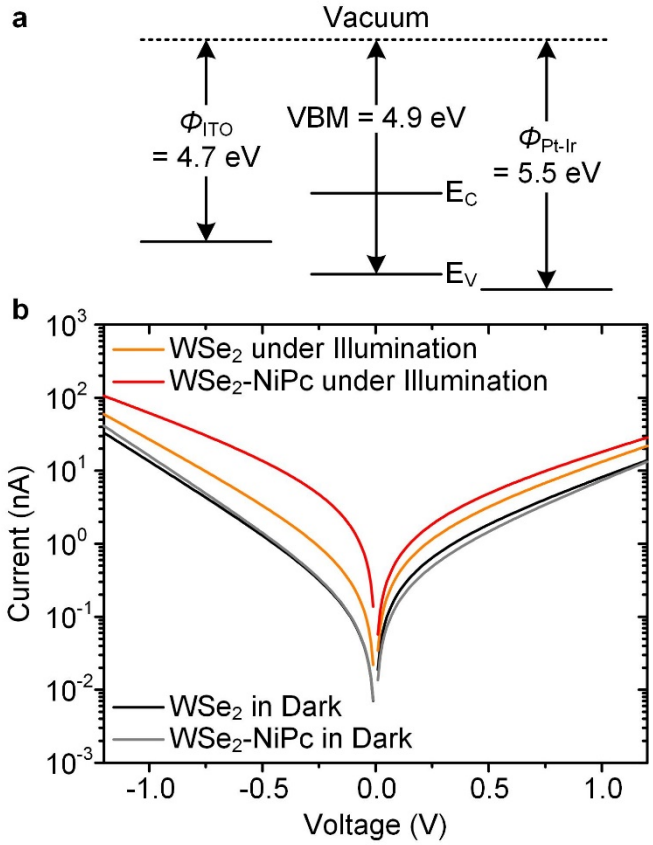

Figure S16. (a) Energy band diagram of ITO/WSe_2/Pt-Ir, where Φ_{ITO} is the work function of ITO (4.7 eV), VBM of WSe_2 (valence band maximum, ~4.9 eV),[17] and Φ_{Pt-Ir} is the work function of Pt-It probe (5.5 eV). Because Φ_{Pt-Ir} is aligned with the valence band of p-type WSe_2,[18] it forms an ohmic contact, while the Schottky barrier forms between the ITO and the WSe_2. The barrier height can be represented as Φ_B = VBM - Φ_{ITO} and calculated to be ~0.2 eV. (b) Semi-log *I*–*V* plots of WSe_2 and WSe_2-NiPc in dark and under illumination. The each curve is obtained from the fitting result of thermionic emission model.

11. 2D current profiles and PL spectra of WSe_2 and NiPc-functionalized WSe_2

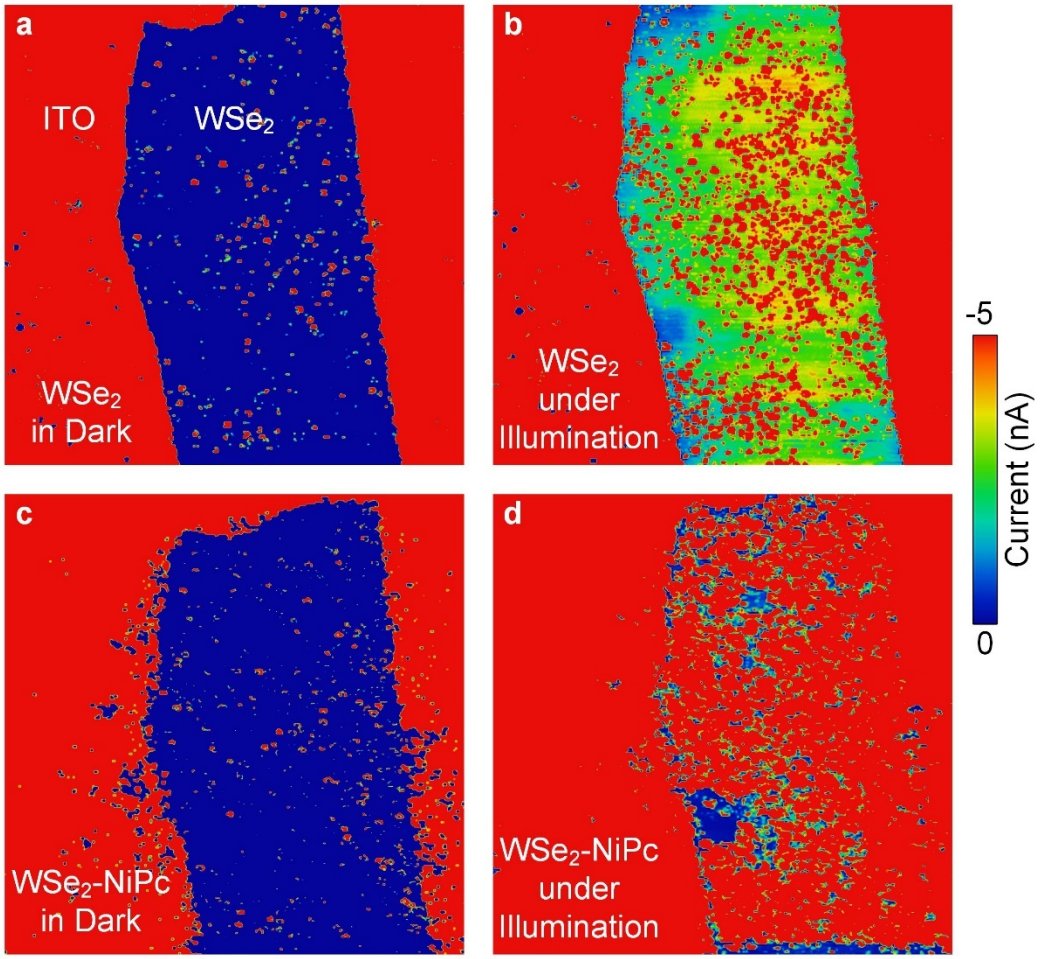

Figure S17. 2D current profiles of (a) WSe_2 in dark, (b) WSe_2 under illumination (λ_{ex} = 658 nm), (c) WSe_2-NiPc in dark, and (d) WSe_2-NiPc under illumination (λ_{ex} = 658 nm). The raster-scanned current profiles were measured by PC-AFM at fixed bias voltage of -0.5 V. These images are used to reconstruct the photocurrent maps by subtracting (a) from (b) for Figure 5e and (c) from (d) for Figure 5f in the main text.

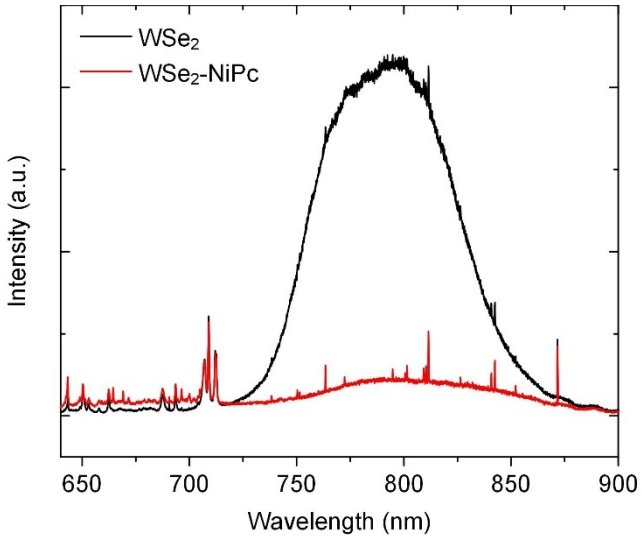

Figure S18. PL spectra of (a) pristine WSe_2 and (b) NiPc-functionalized WSe_2 exfoliated on the ITO substrate. A few Raman signals from the ITO are also shown. Significant PL quenching is observed as expected. The PL quenching is originated from excited electron transfer from the WSe_2 layer to the NiPc molecules, which also contributes to the increased photocurrent after functionalization. It is noted that the spectra were taken from the identical WSe_2 presented in Figure 5d–f and Figure S17.

12. Photocurrent maps and PL spectra of MPc-functionalized TMDCs

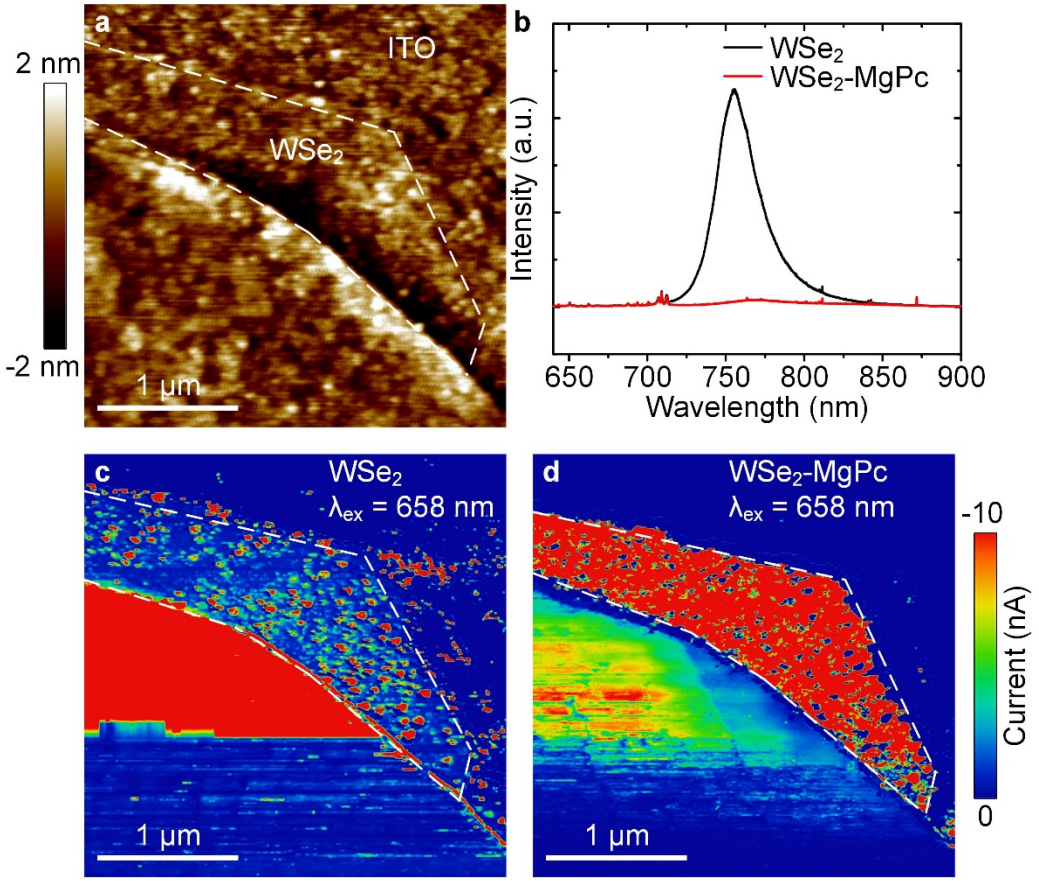

Figure S19. Characterization of WSe_2 before and after MgPc functionalization. (a) AFM height image of WSe_2 exfoliated on an ITO substrate. (b) PL spectra before and after MgPc functionalization, which shows significant PL quenching after functionalization due to excited electron transfer. (c) Photocurrent map of pristine WSe_2 under illumination of 658 nm with a bias voltage of -0.4 V. An average photocurrent is -2.4 ± 0.9 nA. (d) Photocurrent map of MgPc-functionalized WSe_2 measured under the same conditions as the pristine WSe_2. A drastic increase of photocurrent is observed with an average of -15.6 ± 1.9 nA. The PL quenching and increased photocurrent after MgPc functionalization on WSe_2 can be explained by the photoinduced charge transfer mechanism.

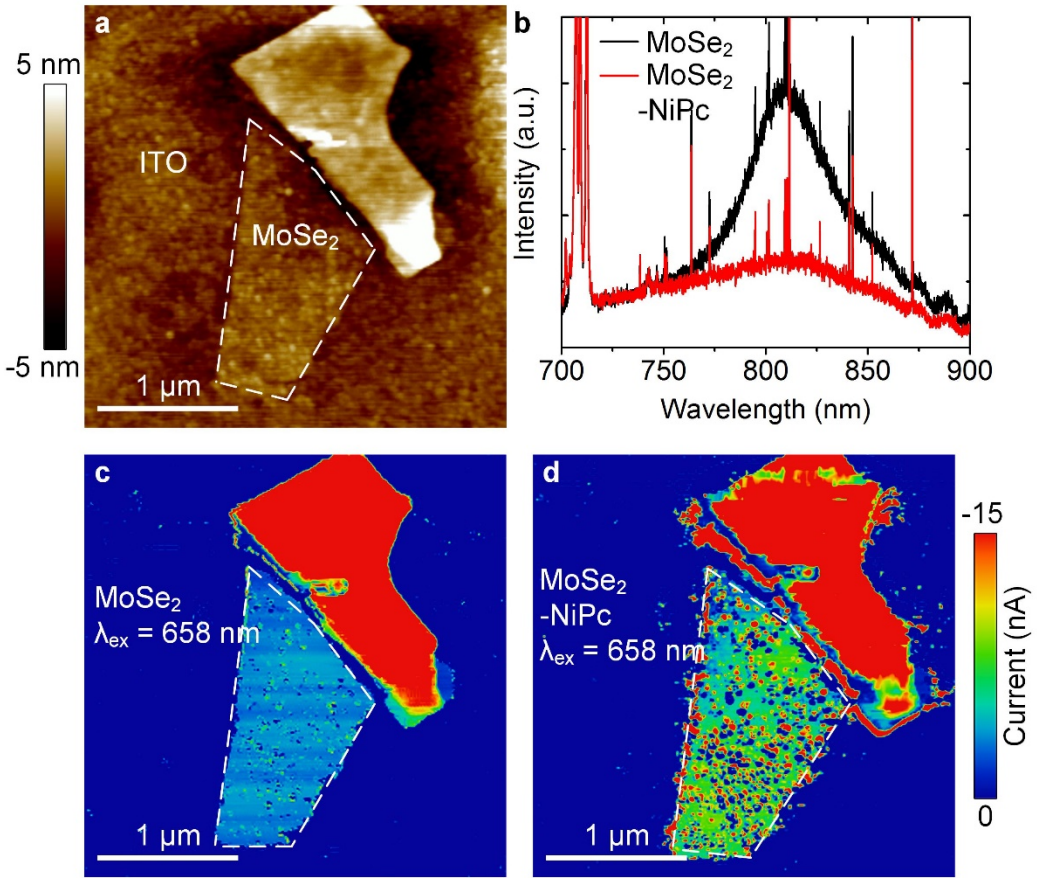

Figure S20. Characterization of $MoSe_2$ before and after NiPc functionalization. (a) AFM height image of $MoSe_2$ exfoliated on the ITO substrate. (b) PL spectra before and after NiPc functionalization, which shows PL quenching after functionalization due to excited electron transfer. (c) Photocurrent map of pristine $MoSe_2$ under illumination of 658 nm with a bias voltage of -0.4 V. An average photocurrent is -4.8 ± 0.5 nA. (d) Photocurrent map of NiPc-functionalized $MoSe_2$ measured under the same conditions as the pristine $MoSe_2$. An increase of photocurrent is observed with an average of -6.3 ± 1.8 nA. The PL quenching and increased photocurrent after NiPc functionalization on $MoSe_2$ can be explained by the photoinduced charge transfer mechanism.

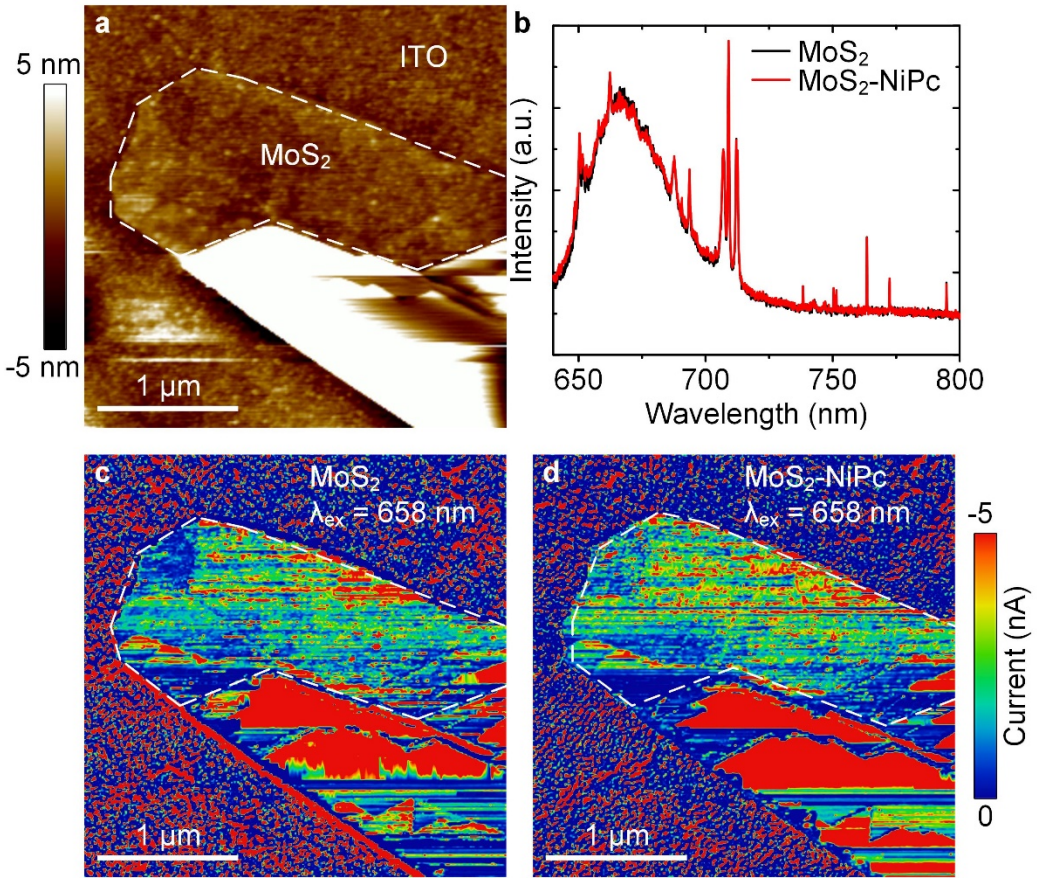

Figure S21. Characterization of MoS_2 before and after NiPc functionalization. (a) AFM height image of MoS_2 exfoliated on the ITO substrate. (b) No significant quenching in PL spectra is observed before and after NiPc functionalization on MoS_2. (c) Photocurrent map of pristine MoS_2 under illumination of 658 nm with a bias voltage of -0.4 V. An average photocurrent is -2.3 ± 0.9 nA. (d) Photocurrent map of NiPc-functionalized MoS_2 measured under the same conditions as the pristine MoS_2. The photocurrent remains nearly the same as that of pristine MoS_2 with an average of -2.4 ± 1.1 nA. This observation is consistent with the photoinduced charge transfer mechanism, where excited electrons from the MoS_2 are not allow to transfer to the NiPc.

13. References

1. Tongay, S.; Zhou, J.; Ataca, C.; Liu, J.; Kang, J. S.; Matthews, T. S.; You, L.; Li, J.; Grossman, J. C.; Wu, J. Broad-Range Modulation of Light Emission in Two-Dimensional Semiconductors by Molecular Physisorption Gating. *Nano Lett*, **2013**, *13*, 2831–2836.
2. Nan, H.; Wang, Z.; Wang, W.; Liang, Z.; Lu, Y.; Chen, Q.; He, D.; Tan, P.; Miao, F.; Wang, X.; Wang, J.; Ni, Z. Strong Photoluminescence Enhancement of MoS_2 through Defect Engineering and Oxygen Bonding. *ACS Nano* **2014**, *8*, 5738–5745.
3. Mouri, S.; Miyauchi, Y.; Matsuda, K. Tunable Photoluminescence of Monolayer MoS_2 via Chemical Doping. *Nano Lett*. **2013**, *13*, 5944–5948.
4. Peimyoo, N.; Yang, W.; Shang, J.; Shen, X.; Wang, Y.; Yu, T. Chemically Driven Tunable Light Emission of Charged and Neutral Excitons in Monolayer WS_2. *ACS Nano* **2014**, *8*, 11320–11329.
5. Lin, J. D.; Han, C.; Wang, F.; Wang, R.; Xiang, D.; Qin, S.; Zhang, X.-A.; Wang, L.; Zhang, H.; Wee, A. T. S.; Chen, W. Electron-Doping-Enhanced Trion Formation in Monolayer Molybdenum Disulfide Functionalized with Cesium Carbonate. *ACS Nano* **2014**, *8*, 5323–5329.
6. Tongay, S.; Suh, J.; Ataca, C.; Fan, W.; Luce, A.; Kang, J. S.; Liu, J.; Ko, C.; Raghunathanan, R.; Zhou, J.; Ogletree, F.; Li, J.; Grossman, J. C.; Wu, J. Defects Activated Photoluminescence in Two-Dimensional Semiconductors: Interplay between Bound, Charged, and Free Excitons. *Sci*. *Rep*. **2013**, *3*, 2657.
7. de Faria, D. L. A.; Constantino, V. R. L.; Baldwin, K. J.; Batchelder, D. N.; Pinnavaia, T. J.; Chibwe, M. Raman Microspectroscopy of Phthalocyanine Intercalates: Ttetrasulphonated Cobalt and Nickel Phthalocyanines in Layered Double Hydroxide. *J*. *Raman Spectrosc*. **1998**, *29*, 103–108.
8. Kahl, J. L.; Faulkner, L. R.; Dwarakanath, K.; Tachikawa, H. Reversible Oxidation and Rereduction of Magnesium Phthalocyanine Electrodes. Electrochemical Behavior and in situ Raman Spectroscopy. *J*. *Am*. *Chem*. *Soc*. **1986**, *108*, 5434–5440.
9. Yang, L.; Majumdar, K.; Liu, H.; Du, Y.; Wu, H.; Hatzistergos, M.; Hung, P. Y.; Tieckelmann, R.; Tsai, W.; Hobbs, C.; Ye, P. D. Chloride Molecular Doping Technique on 2D Materials: WS_2 and MoS_2. *Nano Lett*. **2014**, *14*, 6275–6280.
10. Fang, H.; Tosun, M.; Seol, G.; Chang, T. C.; Takei, K.; Guo, J.; Javey, A. Degenerate n-Doping of Few-Layer Transition Metal Dichalcogenides by Potassium. *Nano Lett*. **2013**, *13*, 1991–1995.
11. McDonnell, S.; Addou, R.; Buie, C.; Wallace, R. M.; Hinkle, C. L. Defect-Dominated Doping and Contact Resistance in MoS_2. *ACS Nano* **2014**, *8*, 2880–2888.
12. McDonnell, S.; Azcatl, A.; Addou, R.; Gong, C.; Battaglia, C.; Chuang, S.; Cho, K.; Javey, A.; Wallace, R. M. Hole Contacts on Transition Metal Dichalcogenides: Interface Chemistry and Band Alignments. *ACS Nano* **2014,** *8*, 6265–6272.
13. Montalti, M.; Credi, A.; Prodi, L.; Gandolfi, M. T. *Handbook of Photochemistry*, 3rd ed.; CRC Press: Boca Raton, Florida, 2006.
14. Zhao, W.; Ribeiro, R. M.; Toh, M.; Carvalho, A.; Kloc, C.; Castro Neto, A. H.; Eda, G. Origin of Indirect Optical Transitions in Few-Layer MoS_2, WS_2, and WSe_2. *Nano Lett*. **2013**, *13*, 5627–5634.
15. Sze, S. M.; Ng, K. K. *Physics of Semiconductor Devices*, 3rd ed.; Wiley-Interscience: Hoboken, New Jersey, 2007.

16. Son, Y.; Wang, Q. H.; Paulson, J. A.; Shih, C.-J.; Rajan, A. G.; Tvrdy, K.; Kim, S.; Alfeeli, B.; Braatz, R. D.; Strano, M. S. Layer Number Dependence of MoS_2 Photoconductivity Using Photocurrent Spectral Atomic Force Microscopic Imaging. *ACS Nano* **2015**, *9*, 2843–2855.
17. Gong, C.; Zhang, H.; Wang, W.; Colombo, L.; Wallace, R. M.; Cho, K. Band Alignment of Two-Dimensional Transition Metal Dichalcogenides: Application in Tunnel Field Effect Transistors. *Appl*. *Phys*. *Lett*. **2013**, *103*, 053513.
18. Fang, H.; Chuang, S.; Chang, T. C.; Takei, K.; Takahashi, T.; Javey, A. High-Performance Single Layered WSe_2 p-FETs with Chemically Doped Contacts. *Nano Lett*. **2012**, *12*, 3788–3792.